

Ore mineralogy and mineral chemistry of the Whale Tail zone, Amaruq gold deposit, Nunavut

Marie-Christine Lauzon¹, Patrick Mercier-Langevin^{2*}, Manon Valette³, Georges Beaudoin¹, Stéphane De Souza³, Olivier Côté-Mantha⁴, and Marjorie Simard⁵

¹Université Laval, 1065 Avenue de la Médecine, Québec, Québec G1V 0A6

²Geological Survey of Canada, 490 rue de la Couronne, Québec, Québec G1K 9A9

³Université du Québec à Montréal, 201 Avenue du Président-Kennedy, Montréal, Québec H2X 3Y7

⁴Agnico Eagle Mines Limited, Exploration Division, 765 chemin de la mine Goldex, Val-d'Or, Québec J9P 7G4

⁵Agnico Eagle Mines Limited, Technical Services, 10200 route de Preissac, Rouyn-Noranda, Québec J0Y 1C0

*Corresponding author's e-mail: patrick.mercier-langevin@canada.ca

ABSTRACT

The 6 Moz Au (190 metric t Au) Amaruq deposit is hosted in a sequence of complexly deformed and metamorphosed chert, graphitic argillite, silicate-facies banded iron formation and mafic-ultramafic volcanic rocks of the Archean Woodburn Lake group in the Kivalliq region of Nunavut. The region was affected by Archean and Paleoproterozoic orogeneses and most Au occurrences are interpreted to be associated with the ca 1.91–1.81 Ga Trans-Hudson event. However, new work indicates that some of the Au may be Early Paleoproterozoic or perhaps even Archean, raising uncertainty about the timing of the Au ore-forming event(s) versus the tectonometamorphic evolution of the region.

The arsenopyrite- and pyrrhotite-dominant Au mineralization of the Whale Tail zone of the Amaruq deposit was sampled from representative drill core to determine the timing of Au introduction relative to the main deformation and associated metamorphism in the study area. Petrography and micro-analyses indicate that the sulphides underwent a complete prograde-retrograde metamorphic cycle, with pre-peak metamorphism Au-rich arsenopyrite being replaced by an assemblage of syn-peak prograde Au-rich löllingite and pyrrhotite. This was followed by retrogression of löllingite to Au-poor secondary arsenopyrite and native Au and electrum inclusions.

INTRODUCTION

Gold deposits of the Kivalliq region of Nunavut are commonly hosted in Neoarchean banded iron formation (BIF). These Au deposits generally consist of contrasting styles of mineralization that are partially to completely hosted in complexly deformed and metamorphosed BIF units (Kerswill, 1993; Dubé and Mercier-Langevin, 2015). This includes world-class Au deposits such as Meliadine (e.g. Lawley et al., 2015a,b; St.Pierre et al., 2020), Meadowbank (Janvier et al., 2015), and Amaruq (e.g. Côté-Mantha et al., 2015, 2017; Mercier-Langevin et al., 2018; Valette et al., 2020) (Fig. 1).

Gold is associated with a crustal-scale fault and its splays at Meliadine (Carpenter and Duke, 2004; Lawley et al., 2015b), with intensely poly-deformed BIF units at the Portage and Goose deposits of the Meadowbank mine (Sherlock et al., 2004; Janvier et al., 2015) and Three Bluffs prospect (Davies et al., 2010), with folded BIFs and steeply dipping high-strain zones and associated shallowly dipping vein systems at Amaruq (Valette et al., 2020). Although Au zones are geometrically controlled by Paleoproterozoic structures pre-

dominantly associated with ca. 1.91–1.81 Ga Trans-Hudson tectonometamorphism (e.g. Hrabi et al., 2003; Pehrsson et al., 2013), recent research reported Re-Os ages as old as 2.3 Ga at Meliadine (Lawley et al., 2015a) and ca. 2.65 Ga at Amaruq (Mercier-Langevin et al., 2018) indicates a more complex, or at least longer (older) hydrothermal history.

The timing of the Au ore-forming event(s) versus the tectonometamorphic evolution at the Whale Tail zone of the Amaruq deposit in eastern Nunavut is determined by documenting the mineralogy and mineral chemistry of the Au-associated sulphides in relation to the regional structural and metamorphic history (Fig. 1). This study provides preliminary constraints on the timing of Au mineralization at Amaruq, documenting that the ore-associated sulphides and Au were introduced before the peak of metamorphism and went through at least one entire prograde-retrograde metamorphic cycle.

Geological Context and Methodology

The Amaruq Au deposit is located in the Kivalliq region of Nunavut, 50 km north of the Meadowbank

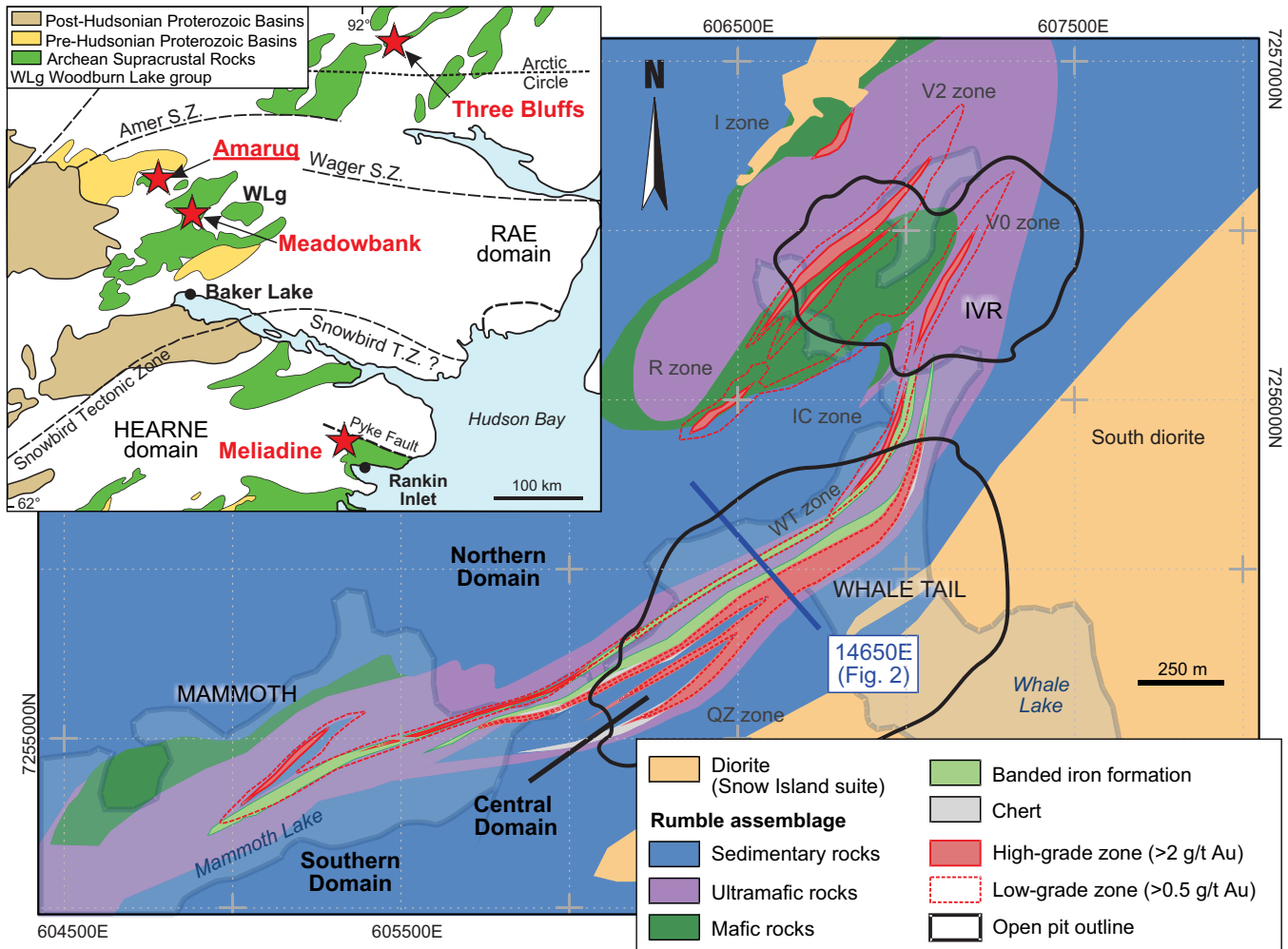


Figure 1. Simplified geological map showing the location and the Amaruq deposit (inset) and the geometry of the main ore zones (modified from Agnico Eagle Mines limited, and Valette et al., 2020). The location of section 14650E (Fig. 2) is also shown. Map coordinates are in UTM NAD83, Zone 14. Abbreviations: S.Z. = shear zone, T.Z. = tectonic zone.

mine (Fig. 1). It is hosted in the ca. 2.73–2.63 Ga metavolcanic and metasedimentary rocks of the Woodburn Lake group (Valette et al., 2020). Note that for conciseness, the prefix “meta” is omitted below. Three main mineralized zones (Whale Tail, IVR, and Mammoth: Fig. 1) have been delineated to date, with commercial production at the Whale Tail zone having officially started in September 2019. Total reserves (proven and probable) and resources (measured, indicated, and inferred) at Amaruq are estimated at 46.4 million metric tonnes of ore at an average grade of 4.08 g/t for a total gold content of 6.08 Moz (189.1 metric tonnes) of Au (Agnico Eagle Mines limited, 2019).

To characterize the ore mineralogy, mineral chemistry, and paragenetic evolution of the sulphide assemblage associated with the gold mineralization at Amaruq, targeted sampling of the altered and mineralized intervals in the Whale Tail zone was completed on core from drillhole IVR14-158. This drillhole has a total length of 303 metres, an azimuth of N146° with a plunge of 70°, and intersected several Au-rich intervals

in the central part of the Whale Tail zone (e.g. 9.97 g/t Au over 6.4 m: Lauzon, 2017; Fig. 2). It is oriented approximately perpendicular to the trend of the units and dominant structural features, such as the principal penetrative planar fabric, but plunges subparallel to the dip of units in that area (Fig. 2). The drillhole intersects mineralized chert, graphitic argillite, and greywacke (Mercier-Langevin et al., 2020), which are part of the central sedimentary package that host most of the ore in the Whale Tail zone. It also intersects BIF and mafic-ultramafic volcanic rocks (Fig. 2).

Several orogenic events are recognized in the region, such as the 2.56–2.50 Ga MacQuoid Orogeny, the 2.56–2.28 Ga Arrowsmith Orogeny, the 1.98–1.91 Ga Taltson-Thelon Orogeny, and the polyphase 1.91–1.81 Ga Trans-Hudson Orogeny (Pehrsson et al., 2013). In the Meadowbank-Amaruq area (Fig. 1), the first phase of metamorphism (M_1), attributed to the Snowbird phase (D_1) of the Trans-Hudson Orogeny is overprinted by the main prograde metamorphic event (M_2) at ca. 1.85–1.83 Ga during the later phase of

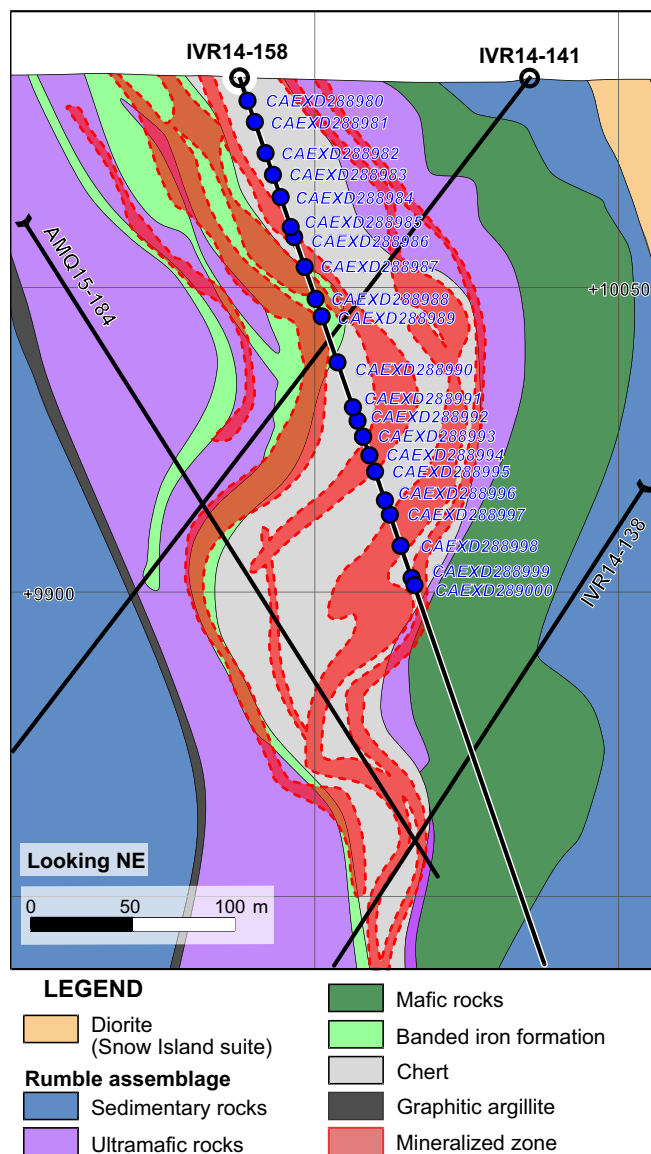


Figure 2. Simplified geological composite section (14,650E \pm 50 m, looking northeast) of the central part of the Whale Tail zone showing the trace of drillhole IVR14-158 and the locations of studied samples. *Modified from Agnico Eagles Mines limited.*

Trans-Hudson deformation (D₂: Pehrsson et al., 2013 and references therein). Readers are referred to Valette et al. (2020) for more information about the structural and metamorphic evolution and potential correlation with regional tectonometamorphic events, nature of the host units, alteration assemblages, and ore zone geometry at Amaruq.

A series of representative samples of the different styles of mineralization was selected for petrographic (transmitted and reflected light microscopy) characterization, electron microprobe analyses, scanning electron microscopy (SEM) analyses (Lauzon, 2017), and whole-rock lithogeochemistry (Mercier-Langevin et al., 2020).

RESULTS

Gangue Mineralogy

The ore intervals in drillhole IVR14-158 are hosted in metasedimentary rocks such as chert (Fig. 3a,b), greywacke, siltstone (Fig. 3c) and mudstone (Fig. 3d), graphitic argillite (Fig. 3e), and silicate-facies iron formation (Fig. 3f). The chert units comprise fine Fe-rich laminae, which can complicate the classification of the units (e.g. chert-rich versus chert-poor BIF: Valette et al., 2020). Ore intervals mostly consist of stratabound to discordant silicification (“silica-flooding”) zones and veins containing variable amounts of ore minerals (e.g. pyrrhotite, arsenopyrite, löllingite, and pyrite; Fig. 3g,h). Only some of the most common gangue minerals (quartz, chlorite, Fe- and Ca-amphiboles, biotite, stilpnomelane, garnet, and andalusite) are presented here, and readers are referred to Valette et al. (2020) for more information.

Quartz is the dominant gangue mineral, and occurs either as a primary component of the host rocks (e.g. detrital quartz in greywacke and microcrystalline quartz in chert) or as a secondary phase associated with alteration and/or veining (e.g. Fig. 3h). It is generally very fine-grained (0.05–2 mm) and shows evidence of recrystallization and deformation, such as undulose extinction. Quartz contains micron-sized silicate mineral inclusions. It is also present in the quartz-carbonate-chlorite veins in the mineralized intervals.

Chlorite is also a common constituent of the gangue. It occurs as bands, often associated with biotite and amphiboles, in both iron formation and chert units (Fig. 3a,b). Chlorite is Fe-rich (ripidolite ((Mg,Fe,Al)₆(Si,Al)₄O₁₀(OH)₈): Lauzon, 2017; Valette et al., 2020).

A range of Fe- and Ca-rich amphiboles is associated with the mineralized intervals (Valette et al., 2020). In BIF and in chert with Fe-rich laminae, grunerite has a prismatic to radial, acicular habit and is associated with biotite. Hornblende forms millimetre-sized isolated crystals, sometimes with biotite coronas. The amphiboles form porphyroblasts that overprint foliated white micas. According to Valette et al. (2020), white micas locally define the S₁ fabric at Amaruq, whereas amphiboles are associated with the M₂ peak metamorphism at upper greenschist facies.

Biotite (siderophyllite (KFe²⁺₂Al(Al₂Si₂O₁₀)(OH)₂): Lauzon, 2017; Valette et al., 2020) is the most common phyllosilicate in the samples studied from drillhole IVR14-158. It is locally present as inclusions in M₂ garnet cores and rims. It is locally aligned along a late crenulation cleavage. In chert units, biotite occurs as randomly oriented porphyroblasts in chlorite-rich bands. Stilpnomelane ((K,Ca,Na)(Fe,Mg,Al)₈(Si,Al)₁₂(O,OH)₃₆·nH₂O) is also a common constituent of the gangue assemblage. It forms elongated, acicular crystals.

tals in the granoblastic matrix of silicified and mineralized zones. It commonly fills the interstices between amphiboles.

Garnet porphyroblasts are present in BIF units. Garnet varies in size from 0.5 to 2 mm and is generally strongly fractured, poikiloblastic, and zoned, and contains micrometre-sized inclusions of magnetite, pyrrhotite, and silicates. Silicate inclusions define a pre-metamorphic peak fabric, whereas rims overprint that fabric, suggesting that garnet growth (and peak metamorphism) occurred syn- to late-D₂ deformation. Garnet varies in composition from the core to the rim. In samples from the IVR14-158 drillcore, the analyzed garnet cores are richer in Al and the rims are richer in Mn. In general, garnet has higher Mn content in BIF units and higher Al content in chert units (Lauzon, 2017).

Andalusite is locally present in the sedimentary rocks and is aligned parallel to a spaced cleavage that overprints the S₂ fabric, indicating a late metamorphic overprint (D₃ deformation: Valette et al., 2020). Post-D₂ retrogression is indicated by partial replacement of biotite by chlorite. Other gangue minerals (not described in detail in this study) such as epidote, tourmaline, titanite, albite, calcite, nickeline, and Cr-spinel are locally to commonly developed in the mineralized intervals, depending on the mineralization style and host rock.

Ore Mineralogy and Mineral Chemistry

Mineralized intervals at Amaruq, and especially in the Whale Tail zone, are directly associated with arsenopyrite and/or pyrrhotite-bearing intervals (e.g. Valette et al., 2020), and are considered very good visual indicators of potential high-grade Au mineralization (e.g. Fig. 3f,g,h). Therefore, the following section focusses on these two minerals and the most commonly associated phases, i.e., löllingite, pyrite, and electrum. Other phases commonly spatially associated with ore intervals, which can vary with host-rock composition, include chalcopyrite, gersdorffite, pentlandite, violar-

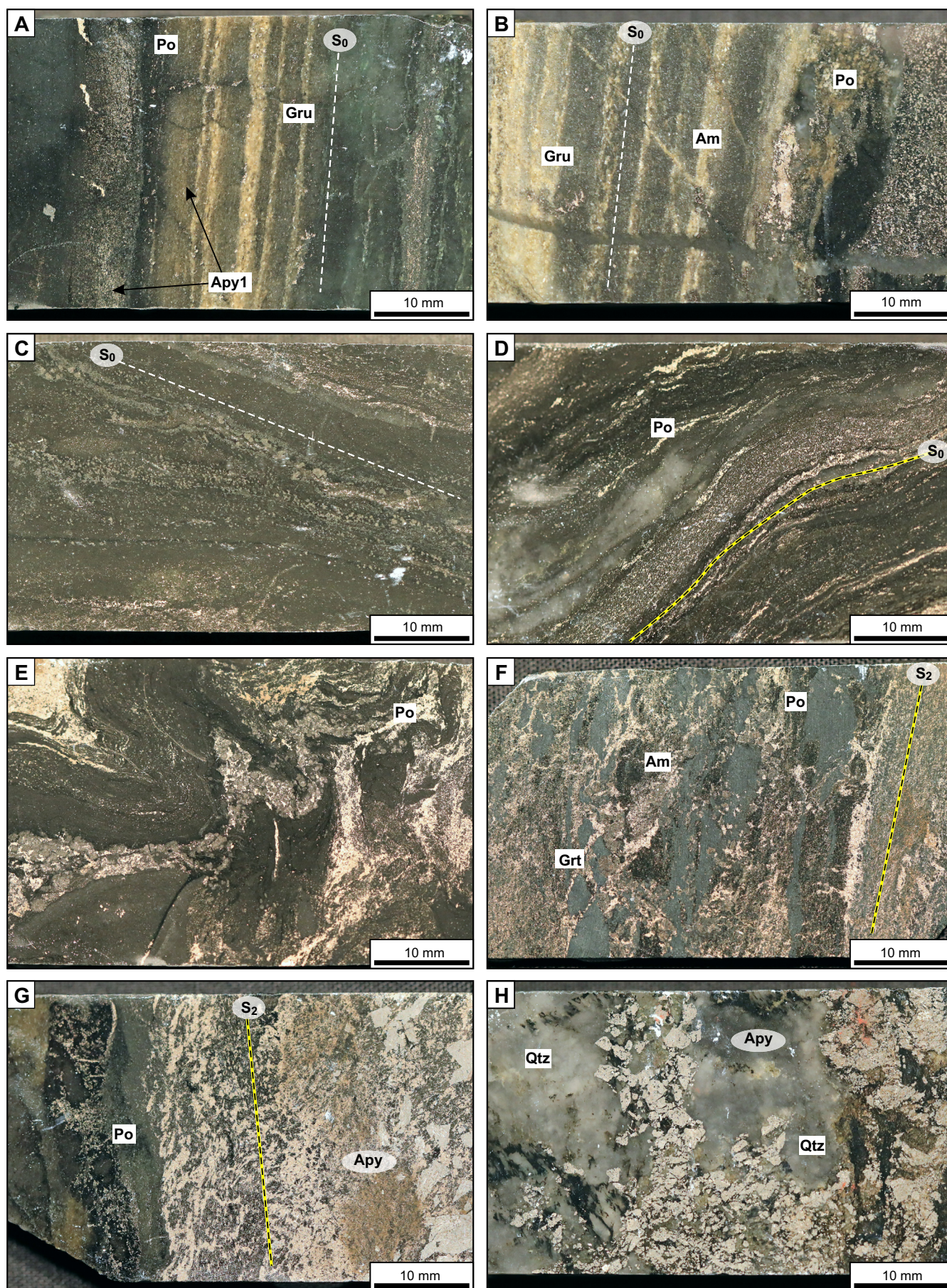
ite, cobaltite, magnetite, ilmenite, scheelite, hessite, tourmaline, and titanite (Lauzon, 2017; Guillevic, 2019; Valette et al., 2020).

Arsenopyrite

Three types of arsenopyrite were documented, mostly based on textural relationships. Type 1 is fine grained (<0.5 mm) and occurs as isolated or disseminated idiomorphic grains (Fig. 4a,b). Type 2 consists of ≤2 mm, hypidiomorphic and idioblastic crystals often forming clusters in siliceous zones and quartz veins (Fig. 3h). Type 3 consists of relatively coarse (1–8 mm), heterogeneous grains or clusters with irregular edges and abundant pyrrhotite and löllingite inclusions (Fig. 3g, 4c). Arsenopyrite of the third type appears to be in equilibrium with the other two minerals as evidenced by triple junctions at the interface between grains (Lauzon, 2017). None of the three types of arsenopyrite appear to be zoned. Native Au (>75 wt% Au and <25 wt% Ag) and/or electrum (<75 wt% Au and >25 wt% Ag) grains commonly occur as inclusions along the margins of the arsenopyrite grains or in fractures. The contrasting arsenopyrite textures, the association with löllingite and pyrrhotite, and the presence of large idioblastic grains suggest recrystallization of arsenopyrite, which is in agreement with the complex element distribution discovered in some crystals by laser ablation inductively-coupled plasma mass spectrometry mapping (Mercier-Langevin et al., 2018).

Microprobe analyses by wavelength dispersive X-ray spectroscopy (WDS) show the presence of invisible Au in all three types of arsenopyrite, although results are commonly close to the detection limit (Table 1). Arsenopyrite types 1 and 2 contain higher Au values on average (101 and 257 ppm, respectively: Lauzon, 2017) than type 3, which is generally below the detection limit. Gold concentrations in type 1 arsenopyrite vary between 29 and 182 ppm (Table 1); although only one analysis is available for type 2 arsenopyrite, it is the highest Au concentration obtained in arsenopyrite from this study. Gold values in type 3 arsenopyrite vary

Figure 3 (opposite page). Photographs of the principal host lithologies and representative examples of mineralized rock inter-sections in drillhole IVR14-158. **a)** Sample CAEXD288990: barren (21 ppb Au), finely bedded chert with thin Fe-rich (amphiboles±oxides) laminae, with small amounts of disseminated pyrrhotite (from a 0.01 g/t Au over 1.5 m interval). **b)** Sample CAEXD288984: barren (59 ppb Au), finely bedded chert and amphibole-rich layers with small amounts of disseminated pyrrhotite and larger pyrrhotite grains (from a 0.28 g/t Au over 1.5 m interval). **c)** Sample CAEXD288992: barren (59 ppb Au), crudely bedded siltstone (from a 0.05 g/t Au interval). **d)** Sample CAEXD288995: barren (36 ppb Au), laminated mudstone with disseminated pyrrhotite (from a 0.07 g/t Au over 1.2 m interval). **e)** Sample CAEXD288998: barren (45 ppb Au), pyrrhotite-rich graphitic argillite (from a 0.11 g/t Au over 1.5 m interval). **f)** Sample CAEXD288989: mineralized (839 ppb Au), pyrrhotite-rich silicate-facies (amphibole-rich) banded iron formation with Mn-rich garnet porphyroblasts (from a 5.99 g/t Au over 0.9 m interval). **g)** Sample CAEXD288999: Au-rich (15,100 ppb Au), silicified chert with abundant pyrrhotite and granoblastic arsenopyrite (from a 5.97 g/t Au over 0.6 m interval). **h)** Sample CAEXD288985: Au-rich (27,200 ppb Au), massively silicified chert and/or diffuse quartz vein with abundant coarse-grained arsenopyrite (from a 25.5 g/t Au over 0.9 m interval). Gold concentrations (in ppb) from Mercier-Langevin et al. (2020). Assay values (in g/t) from Agnico Eagles Mines Limited. See Figure 2 for drillhole IVR14-158 and sample locations. Abbreviations: Am = Ca-Fe amphiboles, Apy = arsenopyrite, Grt = garnet, Gru = grunerite, Po = pyrrhotite, Qtz = quartz/chert, S₀ = bedding, S₂ = main foliation.



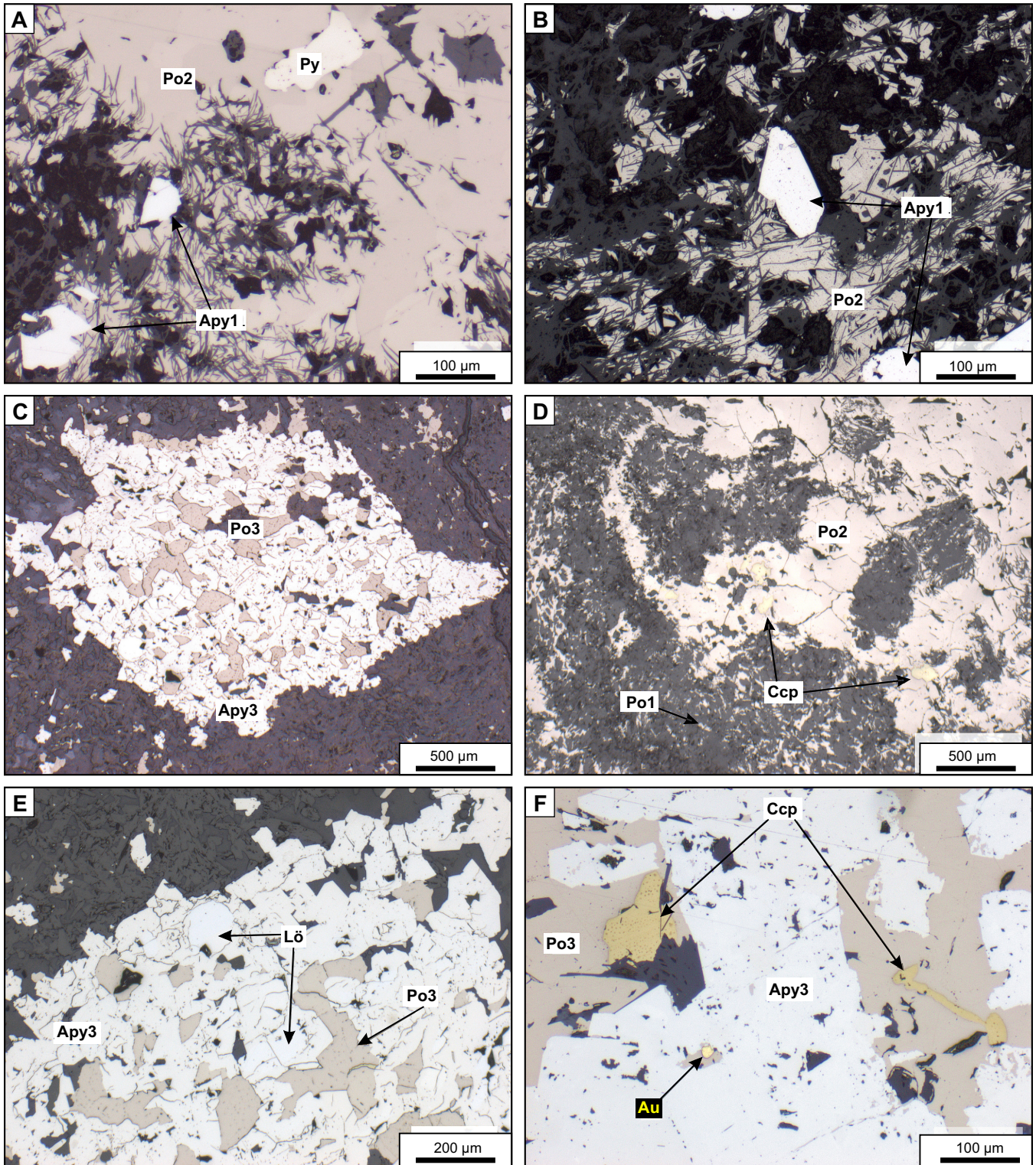


Figure 4. Photomicrographs (reflected light) of mineralized samples. **a)** Sample CAEXD288985: type 1 arsenopyrite crystals in a large mass of pyrrhotite (Po2). **b)** Sample CAEXD288985: type 1 arsenopyrite crystals in disseminated pyrrhotite. **c)** Sample CAEXD288991: aggregate (pseudomorph?) of type 3 arsenopyrite and type 3 pyrrhotite. **d)** Sample CAEXD288988: large, type 2 pyrrhotite mass close to disseminated, type 1 fine pyrrhotite. **e)** Sample CAEXD288991: aggregate (pseudomorph?) of type 3 arsenopyrite and type 3 pyrrhotite with small (<200 µm) löllingite. **f)** Sample CAEXD288985: type 3 arsenopyrite and type 3 pyrrhotite with chalcopyrite and small (<20 µm) free Au or electrum grains. Abbreviations: Apy = arsenopyrite, Au = gold, Ccp = chalcopyrite, Lö = löllingite, Po = pyrrhotite, Py = pyrite.

Table 1. Microprobe analyses of arsenopyrite from drillhole IVR14-158, Whale Tail zone, Amaruq deposit, Nunavut.

Phase	Sample Number	Type	Fe (wt%)	S (wt%)	As (wt%)	Ni (ppm)	Co (ppm)	Au (ppm) ¹
Arsenopyrite	CAEXD288984	type 1	34.7	19.1	47.1	338	1498	29 (bdl)
		type 1	34.0	18.8	47.2	530	4005	110
		type 1	34.4	19.6	46.0	71	1384	68
	CAEXD288985	type 1	33.5	19.2	45.5	344	bdl	98
		type 1	34.5	19.5	46.5	62	42	182
		type 3	34.6	18.9	47.1	153	30	8 (bdl)
		type 3	34.9	19.2	46.9	190	36	bdl
		type 3	35.2	19.6	46.5	bdl	bdl	159
		type 3	34.9	18.8	47.9	178	bdl	77
		type 3	34.9	18.8	47.5	229	17	8 (bdl)
	CAEXD288991	type 3	34.1	19.6	45.9	bdl	bdl	19 (bdl)
		type 3	34.2	18.6	47.2	197	bdl	41 (bdl)
		type 2	34.1	18.6	47.7	492	30	257
		type 1	34.4	18.5	47.7	19	bdl	114
		type 1	34.9	19.5	46.3	78	bdl	136

Abbreviations: bdl = below detection limit, wt = weight.

Analytical parameters: Majors (Fe, S, and As) at 15 kV accelerating voltage, 20 nA beam current, 5 µm electron beam, with a counting time of 20 seconds. Traces (Ni, Co, and Au) at 25 kV accelerating voltage, 100 nA beam current, 5 µm electron beam for 60 seconds (Ni and Co) and with a counting time of 100 seconds (Au). Automated five-spectrometer Cameca SX-100 wavelength dispersive X-ray electron microprobe, Université Laval.

¹Detection limit calculated by the Cameca built-in software taking into account the standard known concentration, background and peak intensities, and sample peak and background intensities, plus statistical parameters. Calculated detection limit for Au varied between 40 and 60 ppm. Values below 60 ppm are therefore considered unreliable.

greatly (from below the detection limit to 159 ppm: Table 1); with the exception of one 159 ppm outlier, all analyzed spots are below 80 ppm and therefore very close to the detection limit. This suggests each of these texturally distinct types of arsenopyrite grains has a different history. Nickel and Co concentrations vary greatly in all arsenopyrite types but seem to be lower on average in type 3 arsenopyrite. Cobalt concentration is markedly high in a few samples, perhaps due to host-rock effects (silicified chert with abundant amphiboles).

Pyrrhotite

Three types of pyrrhotite were also defined based on distinct textural and structural features. Type 1 consists of disseminated and stratiform, finely banded pyrrhotite. This pyrrhotite is fine-grained (Fig. 4d). Type 2 occurs as millimetre-sized discordant veinlets or irregular masses. Type 2 pyrrhotite varies in size and shape (Fig. 4d). Type 3 is texturally heterogeneous and coexists with arsenopyrite and löllingite (Fig. 4e). It occurs as inclusions in large crystals of type 3 arsenopyrite and seems to be in equilibrium with the adjacent löllingite and arsenopyrite.

Pyrrhotite is generally devoid of Au (except for a few analyses with a few tens of ppm Au that are too close to detection limit to be considered significant; Table 2). There is no correlation between the presence of Au and type of pyrrhotite or rock type. Nickel is systematically enriched in samples that come from a mineralized BIF interval. Cobalt is also significantly enriched in all pyrrhotite grains from these samples.

Löllingite

Löllingite is only locally present and is less abundant than arsenopyrite and pyrrhotite. It is systematically present as fine inclusions (0.02–0.5 mm) in type 3 arsenopyrite in silicified chert (Fig. 4e). Löllingite is irregular in shape and can be isolated in larger arsenopyrite grains or may be present as clusters of very tiny disseminated grains within arsenopyrite grains. As with arsenopyrite, native Au and/or electrum is commonly spatially associated with löllingite (*see below*).

Löllingite is significantly enriched in Au compared to the other sulphides analyzed in this study. Gold concentration varies between 69 and 452 ppm (Table 3), with an average of 185 ppm. There are no systematic variations among samples, which suggests that it is homogeneously rich in (invisible) Au. The overall low abundance of löllingite, however, means that it does not hold a significant part of the Au budget at ore-zone scale. It is also enriched in Ni relative to arsenopyrite and pyrrhotite.

Pyrite

Pyrite is more abundant in samples collected close to surface (within 50 m of the surface), where it can comprise up to 20 vol.% of the sulphide assemblage. It occurs as veinlets or as disseminated masses that are generally parallel with the foliation. It is sub-idiomorphic to idiomorphic. At greater depth (more than 50 m below the surface), the shape of the pyrite crystals mimics that of nearby pyrrhotite crystals (xenomor-

Table 2. Microprobe analyses of pyrrhotite from drillhole IVR14-158, Whale Tail zone, Amaruq deposit, Nunavut.

Phase	Sample Number	Type	Fe (wt%)	S (wt%)	As (wt%)	Ni (ppm)	Co (ppm)	Au (ppm) ¹
Pyrrhotite	CAEXD288984	Po2	59.4	39.6	bdl	150	3	bdl
		Po2	59.0	39.7	bdl	144	32	bdl
		Po1	59.1	39.7	bdl	49	2	bdl
		Po1	58.3	39.5	bdl	65	29	bdl
		Po1	59.5	39.7	bdl	119	bdl	bdl
	CAEXD288985	Po2	58.5	39.6	bdl	82	bdl	bdl
	CAEXD288988	Po2	58.4	39.4	bdl	1733	63	bdl
		Po2	58.7	39.4	bdl	1898	77	bdl
		Po1	59.0	39.6	bdl	1757	76	22 (bdl)
		Po2	58.5	39.4	bdl	1844	77	54 (bdl)
		Po2	58.5	39.6	bdl	1788	84	bdl
	CAEXD288991	Po2	59.1	39.2	bdl	1906	67	bdl
		Po2	59.0	39.2	bdl	1791	99	12 (bdl)
		Po2	58.6	39.6	bdl	1760	101	47 (bdl)
		Po3	58.8	39.5	bdl	78	bdl	bdl
		Po3	58.9	39.5	0.1	51	bdl	bdl
		Po3	58.4	39.4	bdl	74	bdl	25 (bdl)
		Po3	58.6	39.6	bdl	69	bdl	11 (bdl)
		Po2	58.8	39.4	bdl	50	bdl	bdl
		Po2	58.3	39.6	bdl	52	bdl	bdl
		Po1	59.0	39.4	bdl	15	bdl	16 (bdl)
		Po1	58.9	39.3	bdl	66	bdl	bdl
		Po1	58.6	39.6	bdl	56	bdl	bdl

Abbreviations: bdl = below detection limit, wt = weight.

¹Detection limit calculated by the Cameca built-in software taking into account the standard known concentration, background and peak intensities, and sample peak and background intensities, plus statistical parameters. Calculated detection limit for Au varied between 40 and 60 ppm. Values below 60 ppm are therefore considered unreliable.

phic), suggesting that this preserved pyrite occurred late in the paragenetic sequence. The grains range in size from 0.05 to 0.2 mm.

Pyrite contains little Au, based on the available microprobe analyses (Lauzon, 2017) and is only slightly enriched in Ni. Its trace element composition is very similar to that of pyrrhotite, to which it is generally spatially associated.

Native Au and electrum

Native Au and electrum are common in samples from drillhole IVR14-158, and more particularly in those containing arsenopyrite. It is spatially associated with pyrrhotite and arsenopyrite, most commonly as inclusions (Fig. 4f). Although some native Au and electrum

grains are in fractures in sulphides, they are more commonly located at the löllingite-arsenopyrite interface (Fig. 5a,b). In some cases, it is in the gangue, but generally it is found in very close proximity to sulphides. Gold and electrum grains are rounded to angular in shape and range in size from <1 to 25 µm (Fig. 4f, 5a,b).

Scanning electron microscope (SEM) analyses of native Au and electrum grains show that Au concentration varies between 63.6 and 86.7 wt%, with Ag concentration varying between 13.3 and 36.4 wt% (Table 4). On average, the analyzed grains comprise 73.9 wt% Au and 26.1 wt% Ag (Lauzon, 2017). The Au/Ag ratio varies between 1.75 and 6.52; a range that is typical of orogenic Au deposits (cf. Boyle, 1979).

Table 3. Microprobe analyses of löllingite from drillhole IVR14-158, Whale Tail zone, Amaruq deposit, Nunavut.

Phase	Sample Number	Type	Fe (wt%)	S (wt%)	As (wt%)	Ni (ppm)	Co (ppm)	Au (ppm) ¹
Löllingite	CAEXD288985	Lö	26.1	1.2	71.1	11,669	479	89
		Lö	27.8	1.2	71.5	2310	26	452
		Lö	27.9	1.2	71.3	2701	40	77
		Lö	27.8	1.1	71.2	3814	17	69
	CAEXD288991	Lö	27.7	1.2	71.0	1370	28	147
		Lö	28.0	1.1	71.3	1440	22	160
		Lö	27.5	1.3	70.7	4395	bdl	233
		Lö	27.8	1.0	71.4	10,368	bdl	350
		Lö	27.0	1.2	71.2	10,503	79	89

Abbreviations: bdl = below detection limit; wt = weight.

¹Detection limit for Au varied between 45 and 65 ppm.

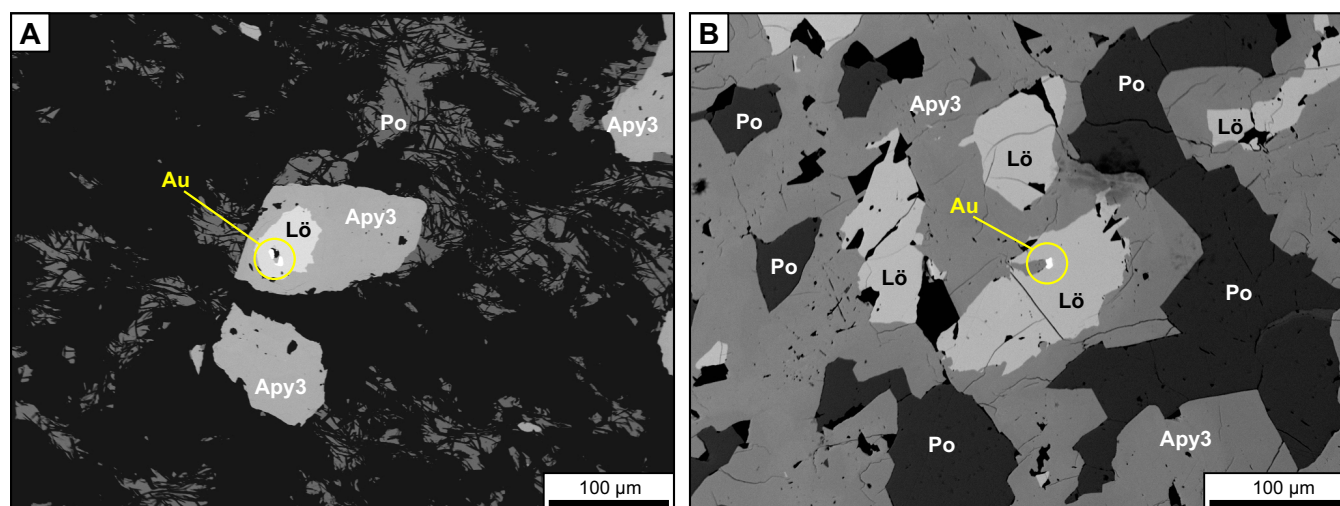


Figure 5. Backscattered electron images of type 3 arsenopyrite with löllingite, pyrrhotite and free gold or electrum. **a)** Sample CAEXD288985: isolated arsenopyrite with a löllingite core containing small Au grains. **b)** Sample CAEXD288991: a large type 3 arsenopyrite with remnant pyrrhotite and isolated löllingite. Free Au occurs at the contact between arsenopyrite and löllingite. Note that löllingite and pyrrhotite are not in contact. Abbreviations: Apy = arsenopyrite, Au = gold, Lö = löllingite, Po = pyrrhotite.

DISCUSSION

Different generations of fabrics related to at least three major deformation events (D_1 to D_3) affect the Amaruq deposit (Valette et al., 2020). The S_1 foliation, which is axial planar to F_1 folds, is affected by tight to closed, gently to moderately, east- to northeast-plunging F_2 folds and associated, moderately southeast-dipping axial planar S_2 schistosity (Valette et al., 2020). On the limbs of F_2 folds, S_1 foliation and S_2 schistosity locally form a composite S_{1-2} fabric. Progressive D_2 strain accommodation led to the development of shear zones that may have been initiated during D_1 deformation. According to Valette et al. (2020), the main fabric (S_2 schistosity) may correspond to the regional D_{p2} 1.91–1.81 Ga Trans-Hudsonian deformation event of Pehrsson et al. (2013). It is not excluded, however, that the main foliation at Amaruq may have originated from the regional S_1 fabric, or even from an earlier Archean

foliation (S_{A2} of Pehrsson et al., 2013), which was subsequently transposed during D_2 deformation.

Petrographic and microstructural relationships between fabrics and metamorphic minerals, such as Mn-garnet porphyroblasts, provide evidence for syn- to late- D_2 peak metamorphism at upper greenschist facies (Valette et al., 2020). Retrogression during D_3 deformation (M_3 of Valette et al., 2020) is evidenced by late phases aligned along the S_3 cleavage in sedimentary rocks. Likewise, sulphide phases show evidence of deformation and metamorphic recrystallization, which indicates that metamorphism overprints and postdates at least part of the mineralizing system.

Type 3 arsenopyrite forms heterogeneous masses with löllingite and pyrrhotite. It contains a lower concentration of invisible Au than arsenopyrite types 1 and 2, which are generally more homogeneous and devoid of löllingite-pyrrhotite inclusions. This suggests that

Table 4. Scanning electron microscopy (SEM) analyses of electrum from drill-hole IVR14-158, Whale Tail zone, Amaruq deposit, Nunavut.

Sample Number	Au		Ag		Note
	(wt%)	(at%)	(wt%)	(at%)	
CAEXD288985	70.48	56.67	29.52	43.33	Contact Apy type 3 and Lö
	68.32	54.15	31.68	45.85	Along Apy type 3
	67.69	53.43	32.31	46.57	Contact Apy type 3 and Lö
	69.07	55.02	30.93	44.98	Inclusion in Apy type 3
CAEXD288991	69.36	55.35	30.64	44.65	Contact Apy type 3 and Lö
	63.56	48.86	36.44	51.14	Inclusion in Apy type 3
	82.20	71.66	17.80	28.34	Contact Apy type 3 and Lö
	76.60	64.19	23.40	35.81	Contact Apy type 3 and Lö
	78.81	67.07	21.19	32.93	Contact Apy type 3 and Lö
	86.73	78.16	13.27	21.84	Inclusion in Apy type 3
CAEXD288997	77.99	65.99	22.01	34.01	Inclusion in Apy type 1
	75.58	62.89	24.42	37.11	Contact Apy type 1 and Lö
	75.15	62.35	24.85	37.65	Contact Apy type 1 and Lö

Abbreviations: Apy = arsenopyrite, at = atomic, Lö = löllingite, wt = weight.

type 3 arsenopyrite formed, at least in part, at the expense of löllingite during retrograde metamorphism, which is in agreement with the laboratory experiments of Tomkins and Mavrogenes (2001) that showed that arsenopyrite resulting from Au-bearing löllingite retrogression contains low levels of invisible Au.

Several authors (e.g. Cathelineau et al., 1989; Morey et al., 2008) have suggested that the solubility of Au in arsenopyrite decreases with increasing temperature. Increasing temperature during prograde metamorphism results in the gradual expulsion of the Au contained in arsenopyrite. This agrees with the observations made of the different types of arsenopyrite and löllingite in samples from drillhole IVR14-158. Type 1 and type 2 arsenopyrites contain high concentrations of Au (120.62 ppm Au on average, $n = 8$), whereas recrystallized arsenopyrite (type 3), which result from retrogression of auriferous löllingite (185 ppm Au on average, $n = 9$), have significantly lower gold concentrations (below the detection limit in most cases).

Based on the progressive stages of evolution of arsenopyrite during metamorphism, as outlined by Tomkins and Mavrogenes (2001), retrograde metamorphism at Amaruq led to an increase in invisible Au concentration in the residual löllingite grains as it reverted to arsenopyrite (Fig. 6). The subsequent conversion of löllingite and pyrrhotite to arsenopyrite during cooling precluded Au to re-enter arsenopyrite structure, concentrating part of it (as electrum) at the löllingite-arsenopyrite interface (Fig. 6), with the rest continuing to diffuse into the remaining löllingite (Fig. 6). As temperature decreased and all the löllingite was consumed to form late, retrograde arsenopyrite, Au was largely expelled from the sulphides. Thus, the replacement of prograde löllingite by retrograde arsenopyrite, as seen in the samples from drillhole IVR14-158, is the main process that led to the presence of native Au and electrum.

The Amaruq Au system is the result of a polyphase tectonometamorphic evolution that may have comprised (1) a simple pre- to early peak metamorphism mineralizing event that was quickly overprinted by increasing metamorphic conditions in a “deep earlier context” (cf. Phillips and Powell, 2009) during Trans-Hudson orogenesis; or (2) a syn-D₂ Trans-Hudson event overprinting a separate and much older mineralizing event. The former interpretation is perhaps the simplest and fits the “Paleoproterozoic Au metallotect” concept of Miller et al. (1994). However, preliminary Re-Os geochronology results suggest a long, protracted hydrothermal history at Amaruq (Mercier-Langevin et al., 2018). This agrees with the work of Lawley et al. (2015a), which demonstrated that mineralization in the Meliadine district resulted from temporally distinct Au events. Ongoing work and analyses (Re-Os, ⁴⁰Ar/³⁹Ar,

U-Pb geochronology, Pb and isotopes, and laser ablation inductively coupled-plasma mass spectrometry element mapping) will help unravel the sequence of events at Amaruq.

In summary, syn-ore (“primary”) Au-bearing arsenopyrite grains were converted to löllingite and pyrrhotite during prograde metamorphism. Gold diffused into löllingite during this process. It was later exsolved from löllingite during retrograde metamorphism, as illustrated in Figure 6. This agrees with the presence of native Au and/or electrum inclusions in the granoblastic gangue silicates that formed during peak metamorphism, which further support the interpretation that a gold mineralizing event predated the syn- to late-D₂ peak metamorphism at Amaruq.

CONCLUSION

Although the results presented here are preliminary, they provide clear evidence for a complex evolution of the Whale Tail gold mineralization, including pre-peak metamorphism, with significant modifications during prograde and retrograde metamorphism. Integrating the results of this study with the ongoing geochronology work and research done on the various aspects of the geology of the deposit will help elucidate the timing and mode of emplacement of the Amaruq Au deposit and help refine exploration models for Au in northern Canada.

FUTURE WORK

More detailed work is underway on the Amaruq ore minerals, including microprobe and scanning electron microscopy (SEM) analyses, laser ablation-inductively coupled plasma-mass spectrometry (LA-ICP-MS) spot analyses and element mapping, Pb and S isotopic analyses, and arsenopyrite Re-Os geochronology to better delineate the signature of the different ore zones and ore styles, and also to better constrain the relative and absolute timing of the ore-forming event(s) and the effects of deformation and metamorphism.

ACKNOWLEDGMENTS

This work results from a B.Sc. thesis by M.-C. Lauzon at Université Laval as part of the Gold Project’s activity G-2.4: Lithological and tectonic controls on Paleoproterozoic BIF-hosted/associated gold. The authors want to thank E. Bédard, E. Rousseau, M. Sciuba, and J. Dubé for scientific and technical support. Thanks to M. Choquette and A. Ferland for their help with micro-analytical work. We thank Agnico Eagle Mines Ltd. for access to the property, drill core and database, and for scientific and logistical support. Thanks to A. Deschênes-Dénoimé, G. Tremblay, and M. Boutin for their help with some of the figures. An earlier version of this report benefited from the reviews

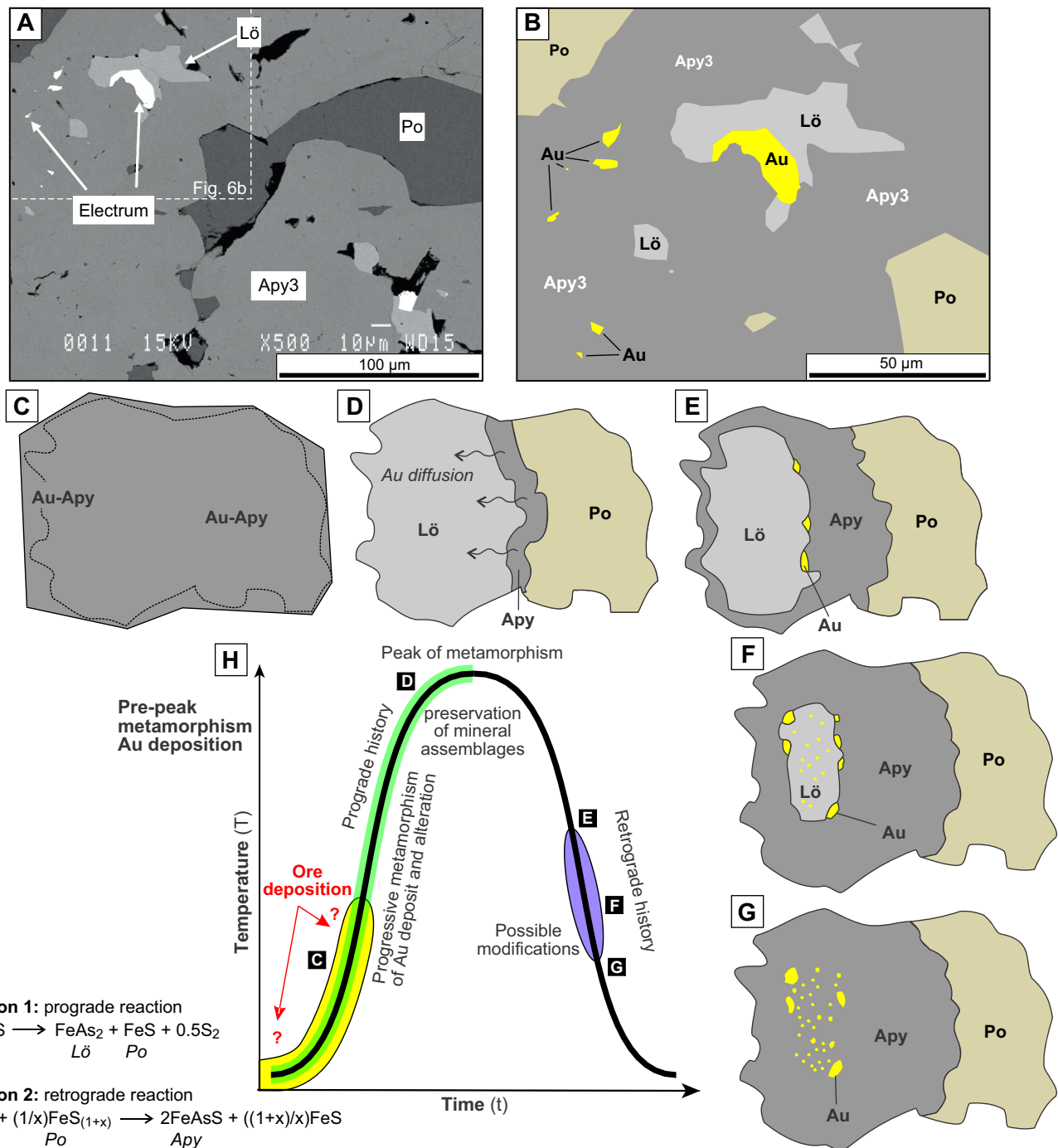


Figure 6. a) Backscattered electron image of type 3 arsenopyrite with löllingite, pyrrhotite, and electrum resulting from retrograde recrystallization of löllingite and liberation of Au. b) Close-up of (a), redrawn to show arsenopyrite, löllingite, electrum, and pyrrhotite relationships. c, d, e, f, and g) Theoretical sketches of the progressive stages of destruction of Au-bearing arsenopyrite and Au-rich löllingite showing how Au is redistributed during a prograde-retrograde metamorphic cycle (modified from Tomkins and Mavrogenes, 2001). c) Syn-ore "primary" Au-bearing arsenopyrite crystal(s). d) Prograde metamorphism of the primary arsenopyrite forming an assemblage of Au-rich löllingite (Au diffusion) and pyrrhotite with or without remnant Au-bearing primary arsenopyrite. e) Early phase of retrograde metamorphism with löllingite reverting to retrograde (Au-poor) arsenopyrite, liberating Au (electrum) that does not re-enter arsenopyrite. f) Advanced retrogression of löllingite, increasing Au concentration in the remaining löllingite and liberating more Au at the interface with retrograde arsenopyrite. This stage is equivalent to what is shown in (a) and (b). g) Complete retrogression of löllingite leaving a residue of native Au (electrum) in late (post-peak metamorphism) arsenopyrite. h) Schematic diagram showing the formation of a gold deposit prior to, or in the early stages of high-grade regional metamorphism and its possible evolution (modified from Phillips and Powell, 2009). Equation 1 is from Barnicoat et al. (1991) and equation 2 is from Neumayr et al. (1993). The prograde-retrograde evolution of Au-bearing arsenopyrite, löllingite, pyrrhotite, and gold is shown along the temperature-time (T-t) curve for reference. Abbreviations: Apy = arsenopyrite, Au = gold, Lö = löllingite, Po = pyrrhotite.

of C. Yakymchuk and S. Castonguay. We also acknowledge E. Ambrose and V. Bécu for their technical reviews and editorial handling.

REFERENCES

- Agnico Eagle Mines Limited, 2019. <<https://www.agnicoeagle.com/English/operations-and-development-projects/reserves-and-resources/default.aspx>> [accessed December 15, 2019]
- Barnicoat, A.C., Fare, R.J., Groves, D.I., and McNaughton, N.J., 1991. Synmetamorphic lode-gold deposits in high-grade Archaean settings; *Geology*, v. 19, p. 921–924.
- Boyle, R.W., 1979. The geochemistry of gold and its deposits; Geological Survey of Canada, Bulletin 280, 584 p.
- Carpenter, R.L. and Duke, N.A., 2004. Geologic setting of the West Meliadine gold deposits, Western Churchill Province, Nunavut, Canada; *Exploration and Mining Geology*, v. 13, p. 49–65.
- Cathelineau, M., Boiron, M.-C., Holliger, P., Marion, P., and Denis, M., 1989. Gold in arsenopyrites: Crystal chemistry, location and state, physical and chemical conditions of deposition; *in* The Geology of Gold Deposits: The perspective in 1988, (ed.) R.R. Keys, W.R.H. Ramsay, and D.I. Groves; Society of Economic Geologists, Monograph 6, p. 328–341.
- Côté-Mantha, O., Gosselin, G., Vaillancourt, D., and Blackburn, A., 2015. Amaruq: A new gold discovery in Nunavut, Canada; NewGenGold 2015 meeting, Extended Abstracts, p. 41–56.
- Côté-Mantha, O., Gosselin, G., Vaillancourt, D., and Blackburn, A., 2017. The Amaruq deposits – Building a customized toolset and using a flexible geomodel: Optimization from discovery to mine development; *in* Proceedings of Exploration 17, (ed.) V. Tschirhart and M.D. Thomas; Sixth Decennial International Conference on Mineral Exploration, 2017, p. 553–567.
- Davies, T., Richards, J.P., Creaser, R.A., Heaman, L.M., Chacko, T., Simonetti, A., Williamson, J., and McDonald, D.W., 2010. Paleoproterozoic age relationships in the Three Bluffs Archean iron formation-hosted gold deposit, Committee Bay greenstone belt, Nunavut, Canada; *Exploration and Mining Geology Journal*, v. 19, p. 55–80.
- Dubé, B. and Mercier-Langevin, P. (ed.), 2015. Targeted Geoscience Initiative 4: Contributions to the Understanding of Precambrian Lode Gold Deposits and Implications for Exploration; Geological Survey of Canada, Open File 7852, 297 p.
- Guillevic, F., 2019. Domaines géométallurgiques dans un gisement aurifère: le cas du dépôt Whale Tail, projet Amaruq, Nunavut; M.Sc. thesis, Université du Québec à Chicoutimi, Chicoutimi, Québec, 192 p.
- Hrabi, R.B., Barclay, W.A., Fleming, D., and Alexander, R.B., 2003. Structural evolution of the Woodburn Lake group in the area of the Meadowbank gold deposit, Nunavut; Geological Survey of Canada, Current Research 2003-C27, 10 p.
- Janvier, V., Castonguay, S., Mercier-Langevin, P., Dubé, B., Malo, M., McNicoll, V.J., Creaser, R.A., De Chavigny, B., and Pehrsson, S.J., 2015. Geology of the banded iron formation-hosted Meadowbank gold deposit, Churchill Province, Nunavut; *in* Targeted Geoscience Initiative 4: Contributions to the understanding of Precambrian lode gold deposits and implications for exploration, (ed.) B. Dubé and P. Mercier-Langevin; Geological Survey of Canada, Open File 7852, p. 255–269.
- Kerswill, J.A., 1993. Models for iron-formation-hosted gold deposits; *in* Mineral Deposits Modeling, (ed.) R.V. Kirkham, W.D. Sinclair, R.I. Thorpe, and J.M. Duke; Geological Association of Canada, Special Paper 40, p. 171–199.
- Lauzon, M.-C., 2017. Empreinte minéralogique et géochimique des minéralisations aurifères de la zone Whale Tail du projet Amaruq; B.Sc. thesis, Université Laval, Québec, Québec, 48 p.
- Lawley, C.J.M., Creaser, R.A., Jackson, S., Yang, Z., Davis, B., Pehrsson, S., Dubé, B., Mercier-Langevin, P., and Vaillancourt, D., 2015a. Unravelling the Western Churchill Province Paleoproterozoic gold metallotect: constraints from Re-Os arsenopyrite and U-Pb xenotime geochronology and LA-ICP-MS arsenopyrite trace element chemistry at the BIF-hosted Meliadine gold district, Nunavut, Canada; *Economic Geology*, v. 110, p. 1425–1454.
- Lawley, C.J.M., Dubé, B., Mercier-Langevin, P., Kjarsgaard, B., Knight, R., and Vaillancourt, D., 2015b. Defining and mapping hydrothermal footprints at the BIF-hosted Meliadine gold district, Nunavut, Canada; *Journal of Geochemical Exploration*, v. 155, p. 33–55.
- Mercier-Langevin, P., Valette, M., De Souza, S., Creaser, R.A., McNicoll, V., Grondin-Leblanc, P., St-Pierre, B., Lauzon, M.-C., Malo, M., Côté-Mantha, O., and Simard, M., 2018. Lithologic controls on Paleoproterozoic BIF-hosted/associated gold: Overview of Re-Os geochronology and Pb isotopes preliminary results; *in* Targeted Geoscience Initiative: 2017 report of activities, volume 1, (ed.) N. Rogers; Geological Survey of Canada, Open File 8358, p. 147–152.
- Mercier-Langevin, P., Lauzon, M.-C., Bécu, V., Lauzière, K., and Côté-Mantha, O., 2020. Whole-rock lithogeochemistry along drill core through the gold-bearing Whale Tail zone, Amaruq deposit, Churchill Province, Nunavut; Geological Survey of Canada, Open File 8708, 1 .zip file.
- Miller, A.R., Balog, M.J., Barham, B.A., and Reading, K.L., 1994. Geology of the Early Proterozoic gold metallotect, Hurwitz Group in the Cullaton-Griffin lakes area, central Churchill structural province, Northwest Territories; Geological Survey of Canada, Current Research 1994-C, p. 135–146.
- Morey, A.A., Tomkins, A.G., Bierlein, F.P., Weinberg, R.F., and Davidson, G.J., 2008. Bimodal distribution of gold in pyrite and arsenopyrite: Examples from the Archean Boorara and Bardoc shear systems, Yilgarn craton, Western Australia; *Economic Geology*, v. 103, p. 599–614.
- Neumayr, P., Cabri, L.J., Groves, D.I., Mikucki, E.J., and Jackman, J.A., 1993. The mineralogical distribution of gold and relative timing of gold mineralization in two Archean settings of high metamorphic grade in Australia; *The Canadian Mineralogist*, v. 31, p. 711–725.
- Pehrsson, S.J., Berman, R.G., and Davis, W.J., 2013. Paleoproterozoic orogenesis during Nuna aggregation: A case study of reworking of the Rae craton, Woodburn Lake, Nunavut; *Precambrian Research*, v. 232, p. 167–188.
- Phillips, G.N. and Powell, R., 2009. Formation of gold deposits: Review and evaluation of the continuum model; *Earth-Science Reviews*, v. 94, p. 1–21.
- Sherlock, R., Pehrsson, S., Logan, A.V., Hrabi, R.B., and Davis, W.J., 2004. Geological setting of the Meadowbank gold deposit, Woodburn Lake Group, Nunavut; *Exploration and Mining Journal*, v. 13, p. 67–107.
- St.Pierre, B., Mercier-Langevin, P., Simard, M., Côté-Mantha, O., Blais, J.-C., Savelle, G., and Malo, M., 2020. Structural controls and relative timing of gold mineralization of the banded iron formation-associated Tiriganiaq deposit, Meliadine district, Ranking Inlet greenstone belt, Nunavut; *in* Contributions to the Understanding of Canadian Gold Systems, (ed.) P. Mercier-Langevin, C.J.M. Lawley, and S. Castonguay; Geological Survey of Canada, Open File 8712 p. 237–250. doi:10.4095/326041
- Tomkins, A.G. and Mavrogenes, J.A., 2001. Redistribution of gold within arsenopyrite and löllingite during pro- and retrograde metamorphism: Applications to timing of mineralization; *Economic Geology*, v. 96, p. 525–534.

Valette, M., De Souza, S., Mercier-Langevin, P., Côté-Mantha, O., Simard, M., Wodicka, N., McNicoll, V.J., and Barbe, P., 2020. Lithological and tectonic controls on banded iron formation-associated gold at the Amaruq deposit, Churchill Province, Nunavut, and implications for exploration; *in* Targeted Geoscience Initiative 5: Contributions to the Understanding of Canadian Gold Systems, (ed.) P. Mercier-Langevin, C.J.M. Lawley, and S. Castonguay; Geological Survey of Canada, Open File 8712, p. 251–266. doi:10.4095/326042

